Theoretical Determination of Rate Constants from Excited-States: Application to Benzophenone

Katsuyuki Shizu, and Hironori Kaji*

Institute for Chemical Research, Kyoto University, Uji, Kyoto 611-0011, Japan

This is an initial version of the manuscript submitted to The Journal of Physical Chemistry Part A (Submission date: January 23, 2021).

ABSTRACT

A cost-effective method of theoretically predicting electronic transition rate constants from the excited-states of molecules is reported. This method is based on density functional theory calculations of electronic states and quantitative rate constant determination with the Fermi golden rule. The method is applied to theoretical determination of the excited-state decay mechanism of photoexcited benzophenone, a representative molecule in materials science, photochemistry, and biochemistry. Calculated rate constants for benzophenone are quantitatively consistent with experimental ones, which validates the reliability of our rate constant calculation. The calculated population dynamics indicate that $S_1 \rightarrow T_2 (\leftrightarrow T_3) \rightarrow T_1 \rightarrow S_0$ is the predominant decay pathway.

INTRODUCTION

Theoretical determination of excited-state decay mechanisms has drawn great attention because of its relevance to materials chemistry, photochemistry, and biological chemistry. Decay pathways in such systems usually involve competition between radiative and nonradiative transitions among different electronic, vibrational, and spin states. Radiative transitions include fluorescence and phosphorescence; nonradiative transitions include internal conversion (IC), intersystem crossing (ISC), and geometry relaxation (GR). Calculation of transition rate constants is an effective approach to theoretically determining excited-state decay paths.[1] From calculated transition rate constants, one can easily determine relevant electronic transitions and rate-determining steps. Furthermore, by solving kinetic equations for excited and ground state populations, one can calculate the time evolution of electronic states and determine intermediate states relevant for predicting dominant decay paths.

When calculating transition rate constants of materials in practical use, we are faced with two questions. (1) Which quantum chemical method will accurately predict molecular properties at low computational cost? (2) Which rate expression is suitable for obtaining reliable rate constants? Although these questions have been debated for many years, there is no definitive solution and different choices have been used for different molecular systems. Density functional theory (DFT)[2] and time-dependent DFT (TD-DFT)[3] have been widely used to predict molecular properties in solution and the solid state. DFT has been used to calculate electronic ground-state molecular geometries and ground-state properties, such as permanent dipole moments and vibrational modes, whereas TD-DFT has been used to calculate electronic excited-state properties, such as transition dipole moments (oscillator strength) and emission and absorption wavelengths. Complete active space self-consistent field (CASSCF)[4-6] and multireference

Møller−Plesset perturbation theory (MRMP)[7-9] are also used for such calculations. CASSCF and MRMP are useful for calculating multiple electron excitations but have higher computational costs than TD-DFT. The purpose of this study is to theoretically calculate single electron excitations, for which TD-DFT is generally favored, especially in materials chemistry. The main advantage of DFT and TD-DFT is that by choosing a suitable functional, we can quantitatively predict molecular properties with a reasonable computational cost. We show here that all experimentally determined rate constants, radiative (fluorescence) and nonradiative decay from S_1 to S_0, radiative decay (phosphorescence) from T_1 to S_0, and ISC from S_1 to T_2, are quantitatively reproduced by cost-effective DFT and TD-DFT calculations with reasonable computation times.

Rate constants for transitions between weakly coupled states can be calculated using the Fermi golden rule.[10] The general expression of the Fermi golden rule is as: $k = \frac{2\pi}{\hbar} \langle \Phi_{init} | \mathcal{H}' | \Phi_{fin} \rangle^2 \rho$, where k denotes the rate constant for an electronic transition between initial and final states, $\langle \Phi_{init} |$ and $\langle \Phi_{fin} |$ are the wave functions of the initial and final states of a molecule, respectively, $\mathcal{H}'$ is the perturbation operator that activates the electronic transition, and ρ is the density of states. The Fermi golden rule is applicable when $\langle \Phi_{init} | \mathcal{H}' | \Phi_{fin} \rangle$ and ρ are calculated. However, calculating $\langle \Phi_{init} | \mathcal{H}' | \Phi_{fin} \rangle$ involves integrals between vibrational wavefunctions and often cannot be performed because of the difficulty of the calculations, especially those involving nonradiative transitions. Alternatively, the semiclassical Marcus expression[11-13] has been used to calculate rate constants. In the Marcus formula, $\langle \Phi_{init} | \mathcal{H}' | \Phi_{fin} \rangle$ is replaced by the electronic coupling between the initial and final electronic states, which can be calculated more easily than $\langle \Phi_{init} | \mathcal{H}' | \Phi_{fin} \rangle$.[14-15] However, the Marcus formula is derived from the fully quantum-mechanical Fermi golden rule by assuming the high-temperature and short-

time limits. These assumptions make the Marcus formula invalid, especially for charge transfer transitions via nuclear tunneling, for which the Fermi golden rule is more suitable.[16-19] Recently, various charge transfer excited states and electronic transitions between them (a kind of nonradiative transition) have received considerable attention in materials chemistry. To develop a method of calculating rate constants applicable to modern materials chemistry, it would be desirable to establish a cost-effective approach to predicting all relevant rate constants by the Fermi golden rule.

The aim of this study is to propose a cost-effective method for theoretically determining excited-state decay paths of molecules. DFT and TD-DFT are used to calculate molecular properties and the Fermi golden rule is used to evaluate transition rate constants. As stated above, TD-DFT and the Fermi golden rule are useful for establishing a method of calculating rate constants for applications in materials chemistry. This method is applied to analyze the excited-state decay mechanism of photoexcited benzophenone (BP), which is a representative molecule in materials chemistry, photochemistry, and biological chemistry. The excited-state decay path of BP has been subject to debate for more than 50 years.[20-33] Some experimental studies on the decay mechanism of photoexcited BP have suggested that a direct $S_1 \rightarrow T_1$ ISC is the main decay path[23-24], whereas others have suggested that an indirect $S_1 \rightarrow$ intermediate states $\rightarrow T_1$ decay path is favored over the direct $S_1 \rightarrow T_1$ pathway. Thus, photoexcited BP is a good example for testing our method of calculating transition rate constants and corroborating the decay paths. In this study, calculated population dynamics based on the calculated transition rate constants suggest that the S_1 of photoexcited BP decays to T_1 via T_2- and T_3-mediated decay channels, which supports experimental observations reported by Yabumoto $et\ al.$[28] and Aloïse $et\ al.$[30] In addition, the transition rate constants are in good agreement with experimental results.

Despite the low computational costs, our method can be used to predict excited-state decay paths of molecules and for quantitative predictions of their rate constants.

COMPUTATIONAL METHODS

Non-radiative and radiative transition rate constants of a molecule are calculated by the Fermi golden rule and wave functions obtained with DFT and TD-DFT methods. B3LYP/6-31G(d) and TD-B3LYP/6-31G(d) methods are used to calculate the electronic ground states and excited states, respectively. Nonradiative transitions between singlet states, S_k and S_l ($k \neq l$; $k, l \geq 0$), occur via S_k-S_l IC. The IC rate constant (k_{IC}) can be obtained by replacing $\mathcal{H}'$ in the Fermi golden rule with the first-order vibronic coupling operator, $\frac{\partial \hat{U}_{en}}{\partial Q_m}$, where $\hat{U}_{en}$ denotes the electron-nuclear potential of the molecule and Q_m denotes the normal coordinate of the mth vibrational mode. Let $k_{IC,m}$ denote the rate constant for the S_k-S_l IC activated by the mth vibrational mode. k_{IC} can be written as the sum of $k_{IC,m}$: $k_{IC} = \sum_{m=1}^{M} k_{IC,m}$, where M is the total number of vibrational modes. $k_{IC,m}$ can be expressed as[34-38]:

$$k_{IC,m} = \frac{2\pi\hbar^3}{\Delta E_{FC}^2} V_m{}^2 P_m, \qquad (1)$$

$$V_m = \left\langle S_k \left| \frac{\partial \hat{U}_{en}}{\partial Q_m} \right| S_l \right\rangle, \qquad (2)$$

$$P_m = \sinh\left(\frac{1}{2}\beta\hbar\omega_m\right) \sum_{v_m^i=0}^{\infty} \exp\left\{-\left(\frac{1}{2}+v_m\right)\beta\hbar\omega_m\right\} \times \{v_m D(\Delta E_{AD} + \hbar\omega_m) + (v_m + 1)D(\Delta E_{AD} - \hbar\omega_m)\}, \qquad (3)$$

where V_m denotes the magnitude of vibronic coupling between S_k and S_l activated by the mth vibrational mode, ΔE_{FC} denotes the difference between the S_0-S_k and S_0-S_l vertical excitation

energies (FC is the abbreviation for Franck–Condon), ΔE_{AD} denotes the adiabatic energy

difference between S_k and S_l, β denotes the inverse temperature ($\beta^{-1} = k_B T$, where k_B is the

Boltzmann constant and $T = 300$ K is the temperature, and ω_m and v_m denote the angular

frequency and vibrational quantum number of the mth vibrational mode, respectively, and

$D(x) = \frac{1}{\pi} \frac{\gamma}{x^2 + \gamma^2}$ denotes the Lorentzian distribution function (γ = fwhm/2 and fwhm = 600 cm^{-1})

describing dephasing effects owing to interactions with surrounding molecules.[38] The value of

the fwhm was originally determined for a tetracene single crystal,[39] which is typical value for a

low molecular weight organic compound. Our calculations reproduced the experimental ISC rate

constant of BP in its single crystal form. ΔE_{FC}, V_m, and ω_m were calculated for the optimized

geometries. P_m contains information regarding the density of the final vibrational states. The

energy-downhill S_k-S_l rate constant is first calculated as k_{IC} and then, the energy-uphill S_k-S_l

rate constant is calculated as $k_{IC}\exp(-\beta\Delta E_{FC}/2)$. The factor 1/2 in the exponential function

means that the position of the transition state along the reaction coordinate is halfway between

the S_k and T_l geometries.[40] Equations 1–3 are also used to calculate nonradiative transition rate

constants between triplet states, T_k and T_l ($k \neq l$; $k, l \geq 1$), by replacing S_k and S_l with T_k and T_l,

respectively, and ΔE_{FC} with the difference between the S_0-T_k and S_0-T_l vertical excitation

energies, and ΔE_{AD} with the adiabatic energy difference between T_k and T_l.

S_k-T_l ($k \geq 0, l \geq 1$) nonradiative transition occurs via S_k-T_l ISC. By replacing $\mathcal{H}'$ in the

Fermi golden rule with a one-electron spin-orbit coupling operator[41] ($\mathcal{H}_{SOC}$), the ISC rate

constant (k_{ISC,M_S}) for the three degenerated triplet sublevels $T_l^{M_S}$ ($M_S = 0, \pm1$) can be written as

$$k_{ISC,M_S} = \frac{2\pi}{\hbar} \left| \langle S_k | \mathcal{H}_{SOC} | T_l^{M_S} \rangle \right|^2 D(\Delta E_{AD}) \tag{4}$$

where ΔE_{AD} denotes the adiabatic energy difference between S_k and T_l. When the $S_k \rightarrow T_l$ nonradiative transition is a downhill energy transition, the $S_k \rightarrow T_l^{M_S}$ rate constant is expressed as k_{ISC,M_S}, whereas the energy-uphill $T_l^{M_S} \rightarrow S_k$ rate constant is expressed as $k_{ISC,M_S} \exp(-\beta \Delta E_{FC}/2)$. Hence, the rate equations for S_k and T_l can be written as

$$\frac{d[S_k]}{dt} = -\left(\sum_{M_S=0,\pm 1} k_{ISC,M_S} \right)[S_k] + \sum_{M_S=0,\pm 1} k_{ISC,M_S} \exp(-\beta \Delta E_{FC}/2)\left[T_l^{M_S}\right] + A \quad (5)$$

$$\frac{d[T_l]}{dt} = \left(\sum_{M_S=0,\pm 1} k_{ISC,M_S} \right)[S_k] - \sum_{M_S=0,\pm 1} k_{ISC,M_S} \exp(-\beta \Delta E_{FC}/2)\left[T_l^{M_S}\right] + B \quad (6)$$

$$[T_l] = \sum_{M_S=0,\pm 1}[T_l^{M_S}], \quad (7)$$

where $[S_k]$, $[T_l]$, and $[T_l^{M_S}]$ denote the respective populations of S_k, T_l, and $T_l^{M_S}$, A denotes the contributions from the electronic states other than $[S_k]$ and $[T_l^{M_S}]$ to $d[S_k]/dt$, and B denotes those to $d[T_l]/dt$. A and B for individual combinations of S_k and T_l are described in detail in the Supporting Information [eqs. (1)–(20)]. We reasonably assume that $T_l^{M_S}$ thermally equilibrates before $T_l \rightarrow S_k$ ISC, that is, $[T_l^{M_S}] = [T_l]/3$ holds, Equations 5 and 6 can be expressed as

$$\frac{d[S_k]}{dt} = -\left(\sum_{M_S=0,\pm 1} k_{ISC,M_S} \right)[S_k] + \frac{1}{3}\left(\sum_{M_S=0,\pm 1} k_{ISC,M_S} \right)\exp(-\beta \Delta E_{FC}/2)[T_l] + A \quad (8)$$

$$\frac{d[T_l]}{dt} = \left(\sum_{M_S=0,\pm 1} k_{ISC,M_S} \right)[S_k] - \frac{1}{3}\left(\sum_{M_S=0,\pm 1} k_{ISC,M_S} \right)\exp(-\beta \Delta E_{FC}/2)[T_l] + B. \quad (9)$$

Let k_{ISC} denote the sum of k_{ISC,M_S},

$$k_{ISC} = \sum_{M_S=0,\pm 1} k_{ISC,M_S} \quad (10)$$

Then, substituting Equation 10 into Equations 8 and 9 gives

8

$$\frac{d[S_k]}{dt} = -k_{\text{ISC}}[S_k] + \frac{k_{\text{ISC}}}{3}\exp(-\beta\Delta E_{\text{FC}}/2)[T_l] + A, \tag{11}$$

$$\frac{d[T_l]}{dt} = k_{\text{ISC}}[S_k] - \frac{k_{\text{ISC}}}{3}\exp(-\beta\Delta E_{\text{FC}}/2)[T_l] + B. \tag{12}$$

Equations 11 and 12 show that k_{ISC} represents the energy-downhill $S_k \rightarrow T_l$ rate constant, whereas $1/3\, k_{\text{ISC}}\exp(-\beta\Delta E_{\text{FC}}/2)$ represents the energy-uphill $T_l \rightarrow S_k$ rate constant. This process is frequently called reverse ISC (RISC). The prefactor 1/3 reflects the thermally equilibrated triplet sublevels and appears in the RISC[42-43] and phosphorescence.[44-46] The factor 1/2 in the exponential function means that the position of the transition state along the reaction coordinate is halfway between the S_k and T_l geometries.[40] In a similar manner, when the $S_k \rightarrow T_l$ nonradiative transition is an energy-uphill transition, $k_{\text{ISC}}\exp(-\beta\Delta E_{\text{FC}}/2)$ represents the energy-uphill $S_k \rightarrow T_l$ ISC rate constant, whereas $1/3\, k_{\text{ISC}}$ represents the energy-downhill $T_l \rightarrow S_k$ RISC rate constant. One can define the effective S_k-T_l SOC constant as:

$$|\text{SOC}| = \sqrt{\sum_{M_S=0,\pm1}|\langle S_k|\mathcal{H}_{\text{SOC}}|T_l^{M_S}\rangle|^2}. \tag{13}$$

From Equations 4, 10, and 13, k_{ISC} is expressed in terms of |SOC| as

$$k_{\text{ISC}} = \frac{2\pi}{\hbar}|\text{SOC}|^2 D(\Delta E_{\text{AD}}). \tag{14}$$

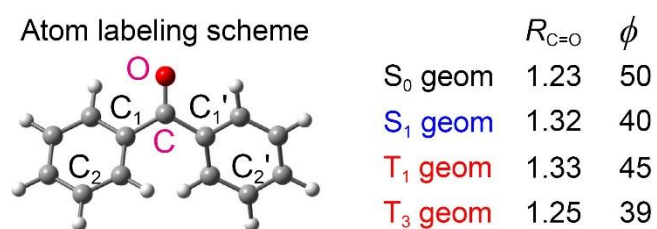Thus, |SOC| represents the strength of the S_k-T_l SOC when $T_l^{M_S}$ is thermally equilibrated.

The S_1-S_0 radiative transition (fluorescence) occurs owing to interactions between the S_1-S_0 transition dipole moment ($\mu_{\text{f},10}$) of a molecule and the electromagnetic field. From the Fermi golden rule, the fluorescence rate constant (k_{f}) can be expressed as $k_{\text{f}} = \frac{4\Delta E_{\text{AD}}^3}{3\hbar^3 c^3}\mu_{\text{f},10}^2$,[47] where ΔE_{AD} is the S_0-S_1 adiabatic energy difference and c is the speed of light. The T_1-S_0 radiative transition (phosphorescence) occurs owing to interactions between the T_1-S_0 transition dipole

moment ($\mu_{p,10}$) and the electromagnetic field. The phosphorescence rate constant (k_p) can be

expressed as $k_p = \frac{4\Delta E_{AD}{}^3}{3\hbar^3 c^3}\mu_{p,10}^2$,[46] where ΔE_{AD} is the S_0-T_1 adiabatic energy difference.

RESULTS AND DISCUSSION

Geometry optimization and frequency analysis for S_0 were performed at the B3LYP/6-

31G(d) level of theory, whereas those for S_1, T_1, T_2, and T_3 were performed at the TD-B3LYP/6-

31G(d) level of theory. Because no imaginary modes were obtained for the optimized S_0, S_1, T_1,

and T_3 geometries, the optimized geometries were confirmed to be local energy minima of S_0, S_1,

T_1, and T_3. The geometry optimization of T_2 resulted in the equilibrium T_1 geometry. Next, the

excitation energies for S_1–S_6 and T_1–T_6 at the S_0, S_1, T_1, and T_3 geometries were calculated using

the TD-B3LYP/6-31G(d) method (Table S10 and Figure S3). Because S_k ($k \geq 2$) and T_l ($l \geq 4$)

were found to be energetically very high (>460 meV) compared with S_1 and T_1-T_3 from the TD-

DFT calculations, only S_0, S_1, and T_1-T_3 are considered in the following discussion. S_1 is

expressed as ^{1}(n,π*)/^{1}(π,π*); T_1 and T_2 are expressed as ^{3}(n,π*)/^{3}(π,π*); and T_3 is expressed as

^{3}(π,π*)/^{3}(n,π*). Here, the notation ^{1}(n,π*)/^{1}(π,π*) means that n,π* and π,π* excitations gave

major and minor contributions to S_1, respectively. In the same way, ^{3}(n,π*)/^{3}(π,π*) means that n-

π* and π-π* excitations make major and minor contributions, respectively, to T_1 and T_2. Figure 1

shows an atom labeling scheme and the calculated carbonyl C=O bond length ($R_{C=O}$), and C_2-C_1-

$C_1{}'$-$C_2{}'$ dihedral angle (ϕ) for the optimized S_0, S_1, T_1, and T_3 geometries of BP. For the S_0, S_1, T_1

(= T_2), and T_3 geometries, $R_{C=O}$ values were calculated to be 1.23, 1.32, 1.33, and 1.25 Å,

respectively, and ϕ as 50°, 40°, 45°, and 39°, respectively. Bond lengths other than the C=O bond

are shown in Figure S1 in Supporting Information. Figure S1 also compares the T_1 geometries

obtained with TD-B3LYP and UB3LYP methods. The calculated bond lengths and ϕ of the two geometries were almost identical, suggesting that both the UB3LYP and TD-B3LTP methods can be used to optimize the T_1 geometry of BP. Figure 2 shows state energy diagrams for BP at the S_0, S_1, T_1 (and T_2), and T_3 geometries. The S_1 and T_1 geometries have similar energy diagrams, which are unlike the diagrams of the S_0 and T_3 geometries. At the S_0 and T_3 geometries, T_2 and T_3 energy levels are close, whereas they are well separated (> 500 meV) at the S_1 and T_1 geometries. S_1 is located higher than T_3 in the S_0 and T_3 geometries, whereas it is located between T_2 and T_3 in the S_1 and T_1 geometries. Thus, the energy level alignment of S_1, T_2, and T_3 is affected by the molecular geometry. Calculated $|SOC|$ values (Equation 13) between S_1, T_1, T_2, and T_3 are also shown in Figure 2. The $\left| \langle S_k | \mathcal{H}_{SOC} | T_l^{M_S} \rangle \right|$ values are listed in Table S12 in Supporting Information. In contrast to the excited-state energy level alignment, the $|SOC|$ values decrease in the order of S_0-T_1 > S_1-T_2 > S_1-T_1 > S_1-T_3 irrespective of the molecular geometry. Because S_1, T_1, T_2, and T_3 have both (n,π^*) and (π,π^*) character, the S_1-T_1, S_1-T_2, and S_1-T_3 SOCs are non-zero owing to the ^{1}(n,π^*)-^{3}(π,π^*) transitions.[48]

	$R_{C=O}$	ϕ
S_0 geom	1.23	50
S_1 geom	1.32	40
T_1 geom	1.33	45
T_3 geom	1.25	39

Figure 1. An atom labeling scheme and the calculated carbonyl C=O bond length ($R_{C=O}$) and C_2-C_1-C_1'-C_2' dihedral angle (ϕ) for the optimized S_0, S_1, T_1, and T_3 geometries of BP. $R_{C=O}$ are in Å and ϕ are in degrees.
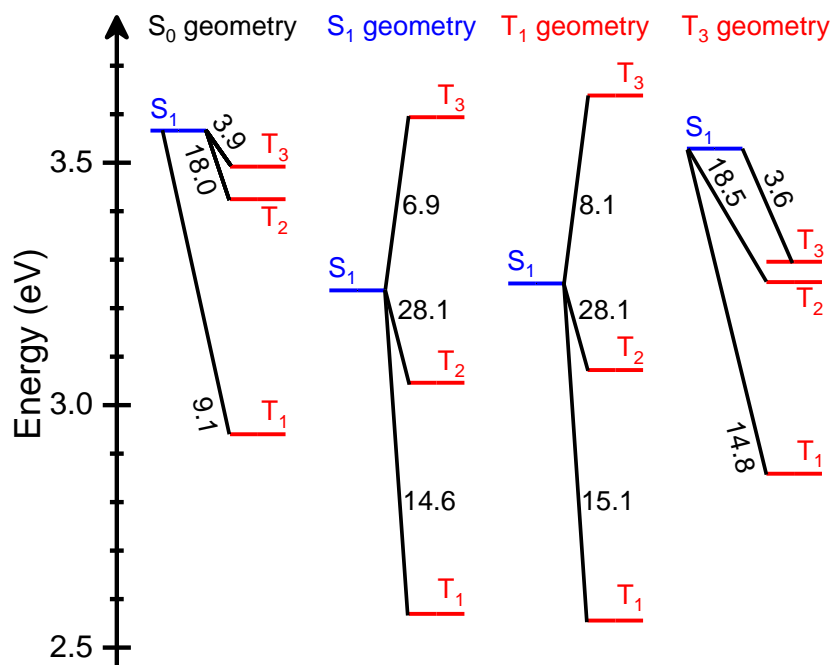
Figure 2. Energy-level diagrams of benzophenone. Numbers are |SOC| (Equation 13) between S_1, T_1, T_2, and T_3 in cm^{-1}. Numerical values of the electronic energies are listed in Table S11. The zero point of the electronic energies is set to be the S_0 energy calculated at the optimized S_0 geometry.

Radiative and nonradiative transition rate constants between S_0, S_1, T_1, T_2, and T_3 calculated for the S_0, S_1, T_1, and T_3 geometries are listed in Table 1. Irrespective of the molecular geometry, the $S_1 \rightarrow T_2$ ISC is the fastest ISC among the ISCs from S_1 because of the large S_1-T_2 SOCs and energetically downhill transition. The calculated $S_1 \rightarrow T_2$ ISC rate constants for the S_1 and T_1 geometries (3.6–3.7×10^{10} s^{-1}) are in excellent agreement with the experimental value for BP single crystals[26] (4×10^{10} s^{-1}). Although they are smaller than those obtained in solution[27, 29-30, 32-33] (6×10^{10}–1.5×10^{11} s^{-1}), the overall agreement between the experimental and calculated values is reasonable. At the S_0 and T_3 geometries, the $S_1 \rightarrow T_3$ ISC is an energetically downhill transition. Hence, the $S_1 \rightarrow T_3$ ISC competes with the $S_1 \rightarrow T_2$ ISC although the S_1-T_3 SOC (4.0 or 3.7 cm^{-1}) is approximately one-fifth of the S_1-T_2 SOC (18.0 or 18.5 cm^{-1}). In contrast, at the S_1 and T_1 geometries, the $S_1 \rightarrow T_3$ ISC is an energetically uphill transition and therefore, the $S_1 \rightarrow T_3$ ISC (1.7 or 1.3×10^7 s^{-1}) occurs much slower than the $S_1 \rightarrow T_2$ ISC (3.6 or 3.7×10^{10} s^{-1}). The calculated $S_1 \rightarrow S_0$ radiative and nonradiative decay rates are of the order of 10^6 s^{-1} and the calculated $T_1 \rightarrow S_0$ radiative decay rates are of the order of 10^2 s^{-1}, irrespective of the molecular geometry. These values are in good agreement with the experimentally obtained values of 10^6 s^{-1} for $S_1 \rightarrow S_0$ radiative decay, $< 10^7$ s^{-1} for $S_1 \rightarrow S_0$ nonradiative decay, and 1.5×10^2 s^{-1} for $T_1 \rightarrow S_0$ radiative decay.[1, 20-21]

Table 1. Nonradiative and radiative transition rate constants (s^{-1}) calculated for the S_0, S_1, T_1, and T_3 geometries of BP.

	S_0 geom	S_1 geom	T_1 geom	T_3 geom	Expt.
Nonradiative transition (ISC)					
$S_1 \rightarrow T_1$	3.1×10^8	8.0×10^8	8.6×10^8	8.2×10^8	
$S_1 \rightarrow T_2$	1.5×10^{10}	3.6×10^{10}	3.7×10^{10}	1.6×10^{10}	4×10^{10} *
$S_1 \rightarrow T_3$	5.6×10^9	1.7×10^7	1.3×10^7	4.8×10^9	
$T_1 \rightarrow S_0$	1.8×10^8	2.0×10^8	2.1×10^8	1.1×10^8	
$T_1 \rightarrow S_1$	5.6×10^2	6.6×10^2	4.1×10^2	6.4×10^2	
$T_2 \rightarrow S_1$	3.2×10^8	3.0×10^8	3.9×10^8	2.6×10^7	
$T_3 \rightarrow S_1$	4.4×10^8	5.7×10^9	7.9×10^9	1.8×10^7	
Nonradiative transition (IC)					
$S_1 \rightarrow S_0$	2.3×10^6	2.0×10^6	2.0×10^6	2.2×10^6	$< 10^7$
$T_1 \rightarrow T_2$	8.5×10^5	7.0×10^5	2.7×10^5	9.8×10^6	
$T_2 \rightarrow T_1$	1.1×10^{10}	7.1×10^9	5.9×10^9	2.0×10^{10}	
$T_2 \rightarrow T_3$	2.0×10^{12}	2.0×10^6	9.6×10^5	2.0×10^{12}	
$T_3 \rightarrow T_2$	7.5×10^{12}	8.1×10^{10}	5.5×10^{10}	4.4×10^{12}	
Radiative decay					
$S_1 \rightarrow S_0$ (fluorescence)	4.5×10^6	3.3×10^6	4.2×10^6	3.7×10^6	10^6
$T_1 \rightarrow S_0$ (phosphorescence)	1.9×10^2	5.1×10^2	5.8×10^2	2.9×10^2	1.5×10^2

* : Value is for single crystals[26]. In solution[27, 29-30, 32-33], $k_{ISC}(S_1 \rightarrow T_2) = 6\times10^{10}–1.5\times10^{11}$ s^{-1}.

To determine decay paths of photoexcited BP, we calculated the time evolution of the S_0, S_1, T_1, T_2, and T_3 populations. Hereafter, if necessary, S_0, S_1, T_1, T_2, and T_3 are written in the form [electronic state]@[optimized geometry] to distinguish each electronic state at each optimized geometry: for example, $S_1@S_0$ denotes the S_1 state for the S_0 geometry. Because we intended to reveal the decay channel from $S_1@S_0$ generated by photoexcitation of the ground state ($S_0@S_0$), the initial population of $S_1@S_0$ was set to be 1 and those of the other states were set to be 0. Note that the total sum of the populations was always 1 at any time point because neither fission nor fusion between electronic states were involved in our population analysis.

Geometry relaxations in S_0, S_1, T_1, T_2, and T_3 can compete with electronic transitions. As stated above, the geometry relaxations in T_2 is eventually deform the molecular geometry to the optimized T_1 geometry. The rate constants of the geometry relaxations (k_{GR}) were unknown and set to a uniform value. From the electronic-transition rate constants and k_{GR}, one can obtain kinetic equations to be solved for calculating the time evolution of the populations (Eqs S1–20 and Table 13 in Supporting Information). The kinetic equations were solved numerically with a time step of 5 fs.

First, we examine decay paths from $S_1@S_0$ without any geometry relaxation ($k_{GR} = 0$ s^{-1}). In this condition, the geometry of BP is fixed to the S_0 geometry and only $S_0@S_0$, $S_1@S_0$, $T_1@S_0$, $T_2@S_0$, and $T_3@S_0$ are populated. Figure 3a shows the calculated populations in the time range of 0–0.5 ns. At first, T_2 and T_3 are populated via the $S_1 \rightarrow T_2$ and $S_1 \rightarrow T_3$ ISCs, because these ISCs are far faster than the $S_1 \rightarrow T_1$ ISC and the $S_1 \rightarrow S_0$ radiative and nonradiative decays (Table 1). To investigate an influence of the $S_1 \rightarrow T_3$ ISC on the population dynamics, we calculated populations by setting the $S_1 \rightarrow T_3$ ISC rate constant to be 0 s^{-1} (Figure 3b). We expected that T_3 would not be populated because the $S_1 \rightarrow T_3$ ISC is forbidden. However, against our expectations, the T_3 population without the $S_1 \rightarrow T_3$ ISC (Figure 3b) was almost as great as that obtained when fast $S_1 \rightarrow T_3$ ISC was allowed (Figure 3a). This result indicates that T_3 is generated by fast $T_2 \rightarrow T_3$ IC after $S_1 \rightarrow T_2$ ISC. Thus, T_3 is involved in the decay mechanism irrespective of the presence of the $S_1 \rightarrow T_3$ ISC. Experimental observations of T_3 would be difficult because of the similar time evolution of the populations and small T_2-T_3 energy difference of 67 meV. Improved energy resolution (for example, through the use of picosecond transient absorption spectroscopy) would enable direct detection of the simultaneous generation of T_2 and T_3.

Next, T_1 is populated via the $T_2 \rightarrow T_1$ IC (Figure 3c). The T_2 and T_3 populations take their maximum values of 0.43 and 0.12, respectively, at $t \approx 0.1$ ns and almost vanish when $t \approx 1$ ns, whereas the T_1 population takes its maximum value of 0.91 at $t \approx 0.5$ ns. After 0.2 ns, the T_1 $\rightarrow S_0$ ISC also occurs and S_0 is increased. Figure 3d shows calculated populations in the time range of 0–35 ns. After $t = 1$ ns, the $T_1 \rightarrow S_0$ ISC occurs mainly and T_1 almost completely decays to S_0 when $t = 25$ ns (at $t = 25$ ns, the populations of T_1 and S_0 are 0.01 and 0.99, respectively). Thus, without any geometry relaxation, the dominant decay paths are the indirect $S_1 \rightarrow T_2$ ($\leftrightarrow$ T_3) $\rightarrow T_1 \rightarrow S_0$ channels (one channel is without T_3 and the other is with T_3, both channels are shown as Type A in Figure 4). The so-called direct mechanism via the $S_1 \rightarrow T_1$ ISC (rate of 3.1×10^8 s^{-1}) is suppressed by the faster $S_1 \rightarrow T_2$ ISC (rate constant is 1.5×10^{10} s^{-1}).
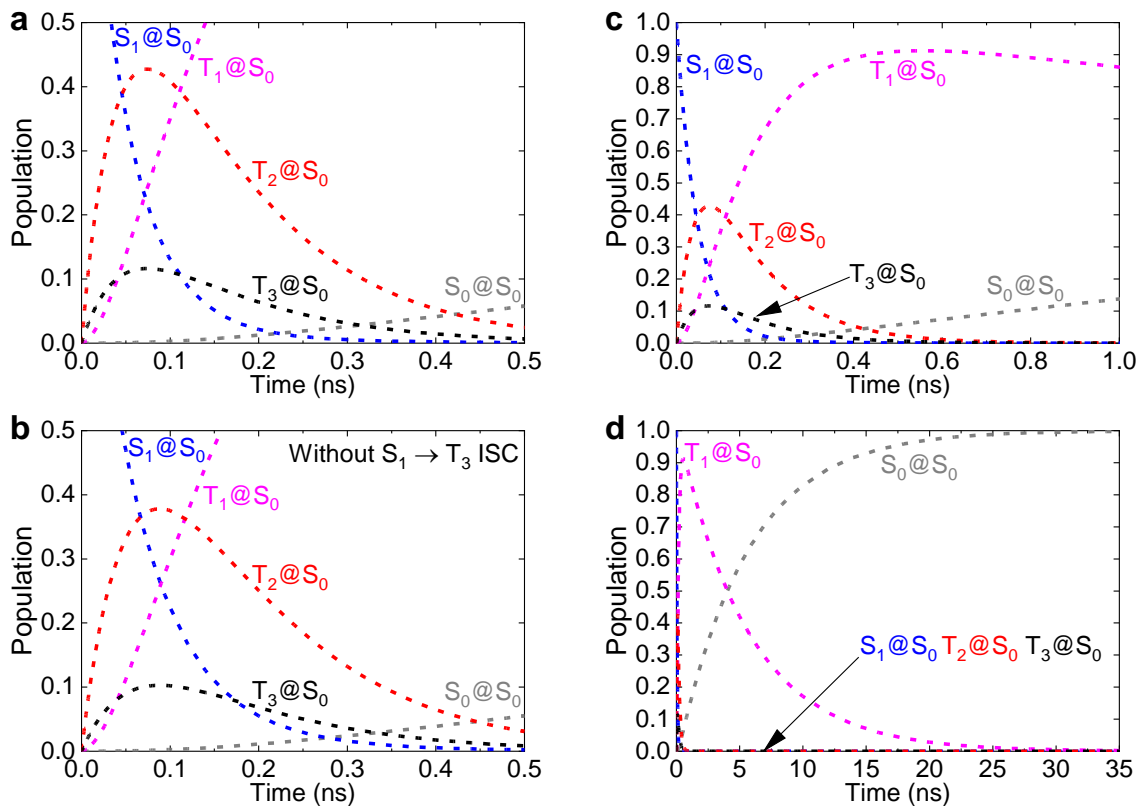
Figure 3. Calculated populations when $k_{GR} = 0$ s^{-1} (without any geometry relaxation) in the time range of (a, b) 0–0.5 ns, (c) 0–1 ns, and (b) 0–35 ns. Figure 3b shows the calculated populations by setting the $S_1@S_0 \rightarrow T_3@S_0$ rate constant to be 0 s^{-1}. $S_1@S_0$, $T_2@S_0$, and $T_3@S_0$ in Figure 3d almost lie on the vertical axis because they are depopulated within 1 ns (Figure 3c) and almost zero in the time range of 1–35 ns. The decay mechanism is categorized into the Type-A mechanism in Figure 4.
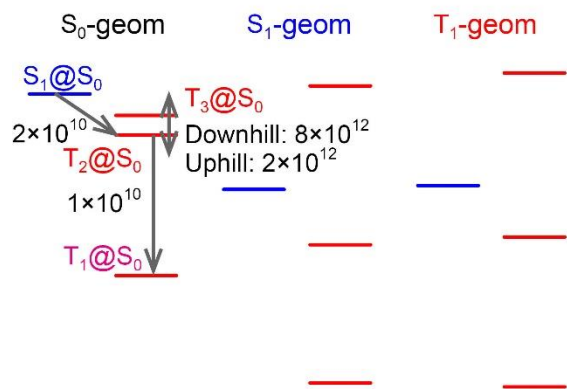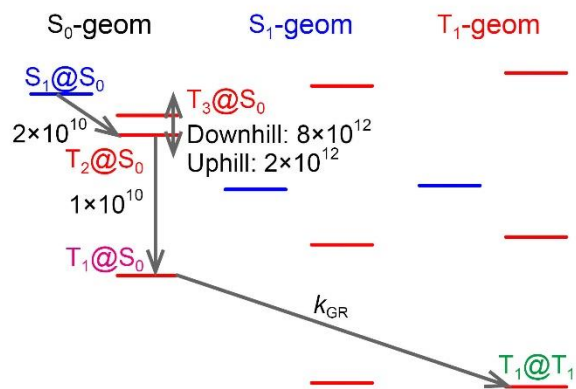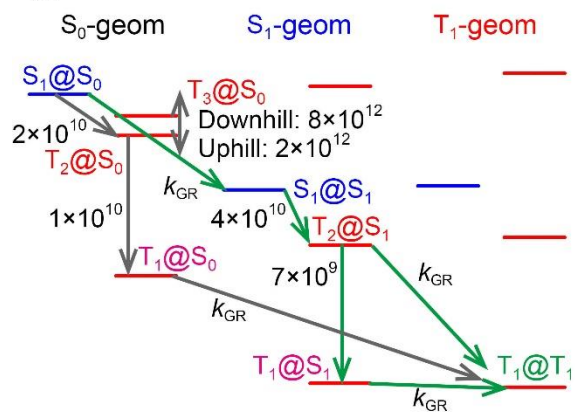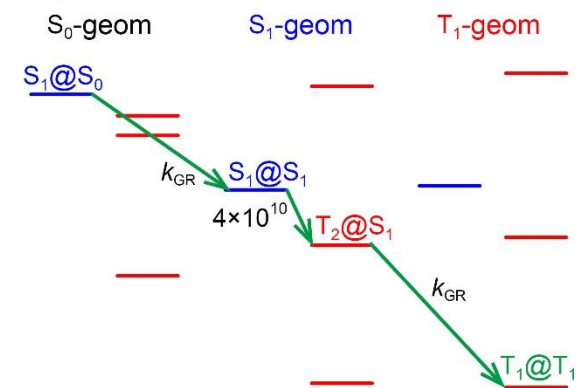
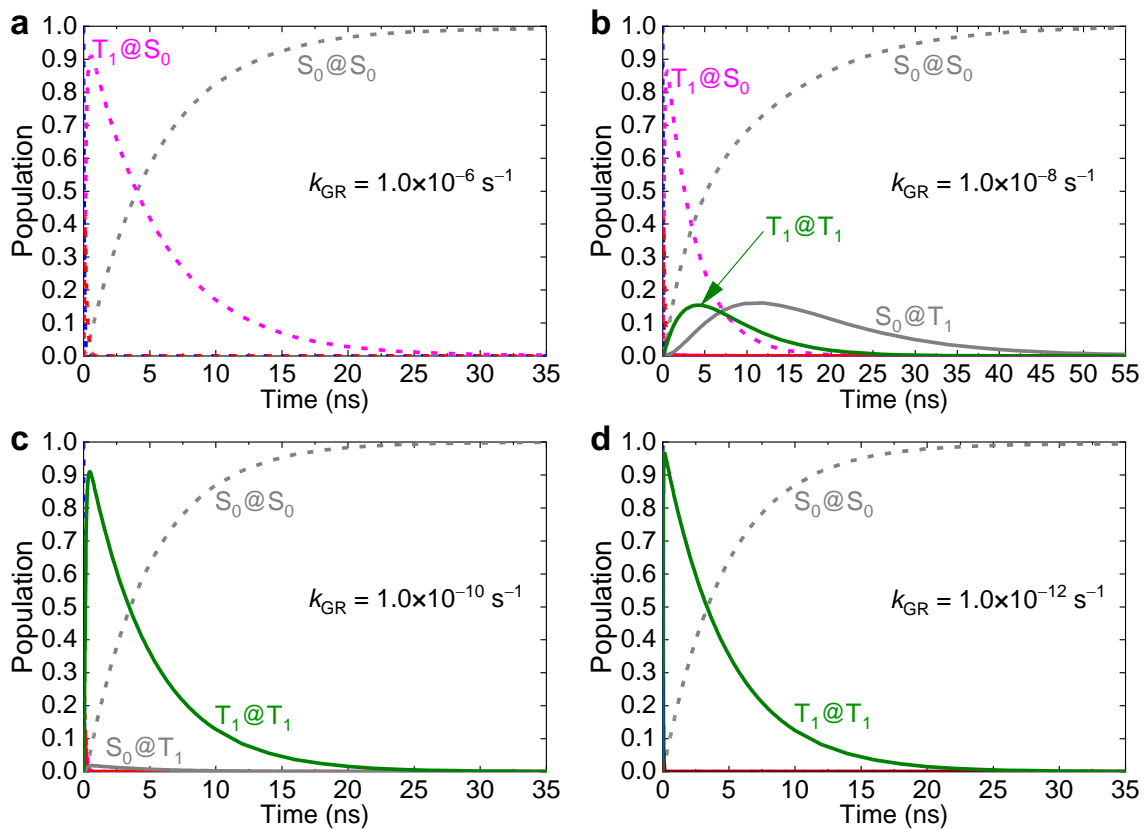**Figure 4.** Dominant T_1 population mechanisms for BP: Type A, B, C, and D. Numbers are rate constants in s^{-1}. $T_2@S_0$ and $T_3@S_0$-mediated decay paths are shown by black arrows; $T_2@S_1$-mediated decay paths are shown by green arrows.

Figure 5. Calculated population dynamics when (a) $k_{GR} = 1.0 \times 10^6$ s^{-1} (Type A), (b) $k_{GR} = 1.0 \times 10^8$ s^{-1} (Type B), (c) $k_{GR} = 1.0 \times 10^{10}$ s^{-1} (Type C), and (d) $k_{GR} = 1.0 \times 10^{12}$ s^{-1} (Type D). Detailed population dynamics in the time range of 0–1 ns are reported in the Supporting Information.

Next, we investigate decay paths considering geometry relaxation. Four cases are examined by varying the k_{GR} values: (1) geometry relaxations occur slower than the relevant ISCs and ICs at the S_0 geometry ($k_{GR} = 1.0 \times 10^6$ s^{-1}); (2) geometry relaxations occur slower than the relevant ISCs and ICs at the S_0 geometry but compete with the $T_1 \rightarrow S_0$ ISC ($k_{GR} = 1.0 \times 10^8$ s^{-1}); (3) geometry relaxations compete with the $S_1 \rightarrow T_2$ ISCs ($k_{GR} = 1.0 \times 10^{10}$ s^{-1}); (4) geometry relaxations occur faster than the relevant ISCs and ICs ($k_{GR} = 1.0 \times 10^{12}$ s^{-1}). From calculated population dynamics, decay pathways depend on k_{GR} (Figure 4).

Figure 5 shows the calculated population dynamics for the four k_{GR} values. The population dynamics in the short time range are reported in detail in the Supporting Information. When (1) $k_{GR} = 1.0 \times 10^6$ s^{-1}, because the $S_1@S_0 \rightarrow S_1@S_1$ geometry relaxation occurs much slower than the $S_1@S_0 \rightarrow T_2@S_0$ ISC (1.5×10^{10} s^{-1}), the molecular geometry is fixed to the S_0 geometry during the electronic transitions and the population dynamics (Figure 5a) are almost identical to those obtained when $k_{GR} = 0$ s^{-1} (Figure 3b). Hence, the decay channel is categorized into Type A (Figure 4). When (2) $k_{GR} = 1.0 \times 10^8$ s^{-1}, because the $T_1@S_0 \rightarrow T_1@T_1$ geometry relaxation competes with the $T_1@S_0 \rightarrow S_0@S_0$ ISC (1.8×10^8 s^{-1}), $S_0@S_0$ and $T_1@T_1$ are simultaneously populated after $T_1@S_0$ is produced (Figure 5b), suggesting that BP takes the S_0 and T_1 geometries and the decay channel is categorized into Type B (Figure 4). When (3) $k_{GR} = 1.0 \times 10^{10}$ s^{-1}, because the $S_1@S_0 \rightarrow S_1@S_1$ geometry relaxation and $S_1@S_0 \rightarrow T_2@S_0$ ISC (1.5×10^{10} s^{-1}) occur in the same time scale, $S_1@S_1$ and $T_2@S_0$ first increase simultaneously. Then, the successive $T_2@S_0 \rightarrow T_1@S_0 \rightarrow T_1@T_1$ and $S_1@S_1 \rightarrow T_2@S_1 \rightarrow T_1@S_1 \rightarrow T_1@T_1$ conversions predominantly occur and $T_1@T_1$ is largely populated (Figure 5c). Thus, BP takes the S_0, S_1, and T_1 geometries and the decay channel is categorized into Type C (Figure 4). When (4) $k_{GR} = 1.0 \times 10^{12}$ s^{-1}, because the $S_1@S_0 \rightarrow S_1@S_1$ geometry relaxation occurs much faster than

competitive ISCs at the S_0 geometry $(3.1 \times 10^8 – 1.5 \times 10^{10}$ s$^{-1})$, the $S_1@S_1$ production is favored

and $S_1@S_0$ is almost completely converted into $S_1@S_1$ within 4 ps. For the population dynamics

in the time range of 0–10 ps, see Supporting Information. After 4 ps, successive $S_1@S_1 \rightarrow$

$T_2@S_1 \rightarrow T_1@T_1$ occurs and $T_1@T_1$ is largely populated (Figure 5d). However, unlike in case

(3) $k_{GR} = 1.0 \times 10^{10}$ s^{-1}, the $T_2@S_0$-mediated decay path is suppressed by the fast $S_1@S_0 \rightarrow$

$S_1@S_1$ geometry relaxation and the decay channel is categorized into Type D (Figure 4).

The decay mechanism of photoexcited BP depends on k_{GR}. When the GR does not occur

and is slow (Type A and B), the decay path is $S_1 \rightarrow T_2 \leftrightarrow T_3 \rightarrow T_1 \rightarrow S_0$. When the GR is

intermediate (Type C), two pathways are possible, $S_1 \rightarrow T_2 \leftrightarrow T_3 \rightarrow T_1 \rightarrow S_0$ and $S_1 \rightarrow T_2 \rightarrow T_1$

$\rightarrow S_0$. When the GR is fast (Type D), the path is $S_1 \rightarrow T_2 \rightarrow T_1 \rightarrow S_0$. Therefore, we conclude

that there are two kinds of decay channels for photoexcited BP; $S_1 \rightarrow T_2 \leftrightarrow T_3 \rightarrow T_1 \rightarrow S_0$

and/or $S_1 \rightarrow T_2 \rightarrow T_1 \rightarrow S_0$. These are is uniformly expressed as $S_1 \rightarrow T_2 (\leftrightarrow T_3) \rightarrow T_1 \rightarrow S_0$.

In this sense, our calculations support the experimentally proposed indirect $S_1 \rightarrow T_2 \rightarrow T_1$ decay

channels[28, 30] among various models as described in the Introduction. This is because the

distinction of T_2 and T_3 is very difficult experimentally owing to the similar time evolution of

their populations (Figure 3) and very close T_2-T_3 energies (Types A – C in Figure 4). The

predicted decay mechanism is reasonably consistent with that determined by more sophisticated

quantum chemical methods based on CASSCF and quantum dynamics methods in that T_2 is

involved as an intermediate state.[32-33] In this study, we did not intended to reject the possibility of

other intermediate states, such as highly excited singlet states. In our present calculations,

multiphoton and multiexciton processes are not included and hence, fission of highly excited

singlet states produced via biphotonic excitation[26] is beyond our consideration.

SUMMARY

We theoretically determined the excited-state decay paths of photo-excited BP and related rate constants on the basis of the cost-effective DFT and TD-DFT calculations and the Fermi golden rule. The excited-state population dynamics and resulting decay mechanism depends on the rate of geometry relaxation. When the rate of the geometry relaxation was slower than 10^8 s^{-1}, BP decays via the $T_2@S_0$ and $T_3@S_0$-mediated paths. In addition, when the rate of geometry relaxation is faster than 10^{10} s^{-1}, BP takes the S_1 geometry and decays via the $T_2@S_1$-mediated pathway. In any case, the dominant decay path involves the indirect $S_1 \rightarrow T_2 \rightarrow T_1$ decay channels. The predicted decay paths were consistent with the experimentally suggested one. In addition, the calculated rate constants are in excellent agreement with experimental results. Our method offers a cost-effective prediction of rate constants and excited decay pathways of molecules. These features are advantageous for theoretical design of novel optoelectronic materials.

ASSOCIATED CONTENT

Supporting Information

Standard nuclear orientations of the optimized S_0, S_1, T_1, and T_3 geometries of BP. Bond lengths and the dihedral angle between the phenyl rings of the optimized S_0, S_1, T_1, and T_3 geometries. HOMO−4, HOMO−3, HOMO−2, HOMO−1, HOMO, LUMO, LUMO+1, LUMO+2, LUMO+3, and LUMO+4 calculated for the optimized S_0, S_1, T_1, and T_3 geometries. Excitation energies of S_0, S_1, T_1, T_2, and T_3 calculated at the S_0, S_1, T_1, and T_3 geometries. Franck–Condon energy differences between S_0, S_1, T_1, T_2, and T_3 calculated for the optimized S_0, S_1, T_1, and T_3 geometries. Adiabatic energy differences between S_0, S_1, T_1, T_2, and T_3. Spin-orbit couplings $\left| \langle S_k | \mathcal{H}_{\text{SOC}} | T_l^{M_S} \rangle \right|$ between S_0, S_1, T_1, T_2, and T_3 calculated for the optimized S_0, S_1, T_1, and T_3 geometries. Population dynamics in the short time range.

AUTHOR INFORMATION

Corresponding Author

Hironori Kaji − Institute for Chemical Research, Kyoto University, Uji, Kyoto 611-0011, Japan; orcid.org/0000-0002-5111-3852; Email: kaji@scl.kyoto-u.ac.jp

Authors

Katsuyuki Shizu − Institute for Chemical Research, Kyoto University, Uji, Kyoto 611-0011, Japan; orcid.org/0000-0002-1835-0418

Author Contributions

K.S. carried out all the theoretical calculations. H.K. planned and supervised the project. All authors contributed to the writing of this manuscript. All authors have given approval to the final version of the manuscript.

Notes

The authors declare no competing financial interest.

ABBREVIATIONS

BP, benzophenone; fwhm, full-width at half-maximum; IC, internal conversion; ISC, intersystem crossing; RISC, reverse intersystem crossing; SOC, spin-orbit coupling.

REFERENCES

1.   Turro, N. J.; Ramamurthy, V.; Scaiano, J. C., *Modern Molecular Photochemistry of Organic Molecules*; University Science Books: Sausalito, 2010.
2.   Parr, R. G.; Yang, W., *Density Functional Theory of Atoms and Molecules*; Oxford University Press: New York, 1989.
3.   Runge, E.; Gross, E. K. U., Density-Functional Theory for Time-Dependent Systems. *Phys. Rev. Lett.* **1984**, *52*, 997.
4.   Siegbahn, P.; Heiberg, A.; Roos, B.; Levy, B., A Comparison of the Super-Ci and the Newton-Raphson Scheme in the Complete Active Space Scf Method. *Physica Scripta* **1980**, *21*, 323-327.
5.   Roos, B. O.; Taylor, P. R.; Sigbahn, P. E. M., A Complete Active Space Scf Method (Casscf) Using a Density Matrix Formulated Super-Ci Approach. *Chem. Phys.* **1980**, *48*, 157-173.
6.   Siegbahn, P. E. M.; Almlöf, J.; Heiberg, A.; Roos, B. O., The Complete Active Space Scf (Casscf) Method in a Newton–Raphson Formulation with Application to the Hno Molecule. *J. Chem. Phys.* **1981**, *74*, 2384-2396.
7.   Hirao, K., Multireference Møller–Plesset Perturbation Treatment of Potential Energy Curve of N2. *Int. J. Quantum Chem.* **1992**, *44*, 517-526.
8.   Hirao, K., Multireference Møller—Plesset Method. *Chem. Phys. Lett.* **1992**, *190*, 374-380.
9.   Hirao, K., Multireference Møller—Plesset Perturbation Theory for High-Spin Open-Shell Systems. *Chem. Phys. Lett.* **1992**, *196*, 397-403.
10.   Dirac, P. A. M., The Quantum Theory of the Emission and Absorption of Radiation. *Proceedings of the Royal Society of London. Series A* **1927**, *114*, 243.
11.   Marcus, R. A., On the Theory of Oxidation-Reduction Reactions Involving Electron Transfer. I. *J. Chem. Phys.* **1956**, *24*, 966-978.
12.   Marcus, R. A., Electrostatic Free Energy and Other Properties of States Having Nonequilibrium Polarization. I. *J. Chem. Phys.* **1956**, *24*, 979-989.
13.   Marcus, R. A., Electron Transfer Reactions in Chemistry. Theory and Experiment. *Rev. Mod. Phys.* **1993**, *65*, 599-610.
14.   Brédas, J.-L.; Beljonne, D.; Coropceanu, V.; Cornil, J., Charge-Transfer and Energy-Transfer Processes in Π-Conjugated Oligomers and Polymers: A Molecular Picture. *Chem. Rev.* **2004**, *104*, 4971-5004.
15.   Samanta, P. K.; Kim, D.; Coropceanu, V.; Brédas, J.-L., Up-Conversion Intersystem Crossing Rates in Organic Emitters for Thermally Activated Delayed Fluorescence: Impact of the Nature of Singlet Vs Triplet Excited States. *J. Am. Chem. Soc.* **2017**, *139*, 4042-4051.
16.   Lee, M. H.; Dunietz, B. D.; Geva, E., Calculation from First Principles of Intramolecular Golden-Rule Rate Constants for Photo-Induced Electron Transfer in Molecular Donor–Acceptor Systems. *J. Phys. Chem. C* **2013**, *117*, 23391-23401.
17.   Lee, M. H.; Geva, E.; Dunietz, B. D., Calculation from First-Principles of Golden Rule Rate Constants for Photoinduced Subphthalocyanine/Fullerene Interfacial Charge Transfer and Recombination in Organic Photovoltaic Cells. *J. Phys. Chem. C* **2014**, *118*, 9780-9789.
18.   Lee, M. H.; Dunietz, B. D.; Geva, E., Donor-to-Donor Vs Donor-to-Acceptor Interfacial Charge Transfer States in the Phthalocyanine–Fullerene Organic Photovoltaic System. *J. Phys. Chem. Lett.* **2014**, *5*, 3810-3816.

19.   Wilcox, D. E.; Lee, M. H.; Sykes, M. E.; Niedringhaus, A.; Geva, E.; Dunietz, B. D.; Shtein, M.; Ogilvie, J. P., Ultrafast Charge-Transfer Dynamics at the Boron Subphthalocyanine Chloride/C60 Heterojunction: Comparison between Experiment and Theory. *J. Phys. Chem. Lett.* **2015**, *6*, 569-575.

20.   Gilmore, E. H.; Gibson, G. E.; McClure, D. S., Absolute Quantum Efficiencies of Luminescence of Organic Molecules in Solid Solution. *J. Chem. Phys.* **1952**, *20*, 829-836.

21.   Gilmore, E. H.; Gibson, G. E.; McClure, D. S., Errata: Absolute Quantum Efficiencies of Luminescence of Organic Molecules in Solid Solution. *J. Chem. Phys.* **1955**, *23*, 399-399.

22.   Batley, M.; Kearns, D. R., The Second Triplet State of Benzophenone. *Chem. Phys. Lett.* **1968**, *2*, 423-425.

23.   El-Sayed, M. A.; Leyerle, R., Low Field Zeeman Effect and the Mechanism of the S1 → T1 Nonradiative Process. *J. Chem. Phys.* **1975**, *62*, 1579-1580.

24.   Ohmori, N.; Suzuki, T.; Ito, M., Why Does Intersystem Crossing Occur in Isolated Molecules of Benzaldehyde, Acetophenone, and Benzophenone? *J. Phys. Chem.* **1988**, *92*, 1086-1093.

25.   Matsushita, Y.; Kajii, Y.; Obi, K., Photochemical Reaction of Excited Benzophenone in the Gas Phase. *J. Phys. Chem.* **1992**, *96*, 4455-4458.

26.   Katoh, R.; Kotani, M.; Hirata, Y.; Okada, T., Triplet Exciton Formation in a Benzophenone Single Crystal Studied by Picosecond Time-Resolved Absorption Spectroscopy. *Chem. Phys. Lett.* **1997**, *264*, 631-635.

27.   Ramseier, M.; Senn, P.; Wirz, J., Photohydration of Benzophenone in Aqueous Acid. *J. Phys. Chem. A* **2003**, *107*, 3305-3315.

28.   Yabumoto, S.; Sato, S.; Hamaguchi, H., Vibrational and Electronic Infrared Absorption Spectra of Benzophenone in the Lowest Excited Triplet State. *Chem. Phys. Lett.* **2005**, *416*, 100-103.

29.   Minns, R. S.; Parker, D. S. N.; Penfold, T. J.; Worth, G. A.; Fielding, H. H., Competing Ultrafast Intersystem Crossing and Internal Conversion in the "Channel 3" Region of Benzene. *Phys. Chem. Chem. Phys.* **2010**, *12*, 15607-15615.

30.   Aloïse, S.; Ruckebusch, C.; Blanchet, L.; Réhault, J.; Buntinx, G.; Huvenne, J.-P., The Benzophenone S1(N,Π*) → T1(N,Π*) States Intersystem Crossing Reinvestigated by Ultrafast Absorption Spectroscopy and Multivariate Curve Resolution. *J. Phys. Chem. A* **2008**, *112*, 224-231.

31.   Miyasaka, H.; Mataga, N., Picosecond Laser Photolysis Studies on the Photoreduction of Excited Benzophenone by Diphenylamine in Solutions. *Bull. Chem. Soc. Jpn.* **1990**, *63*, 131-137.

32.   Sergentu, D.-C.; Maurice, R.; Havenith, R. W. A.; Broer, R.; Roca-Sanjuán, D., Computational Determination of the Dominant Triplet Population Mechanism in Photoexcited Benzophenone. *Phys. Chem. Chem. Phys.* **2014**, *16*, 25393-25403.

33.   Marazzi, M.; Mai, S.; Roca-Sanjuán, D.; Delcey, M. G.; Lindh, R.; González, L.; Monari, A., Benzophenone Ultrafast Triplet Population: Revisiting the Kinetic Model by Surface-Hopping Dynamics. *J. Phys. Chem. Lett.* **2016**, *7*, 622-626.

34.   Kubo, R., Thermal Ionization of Trapped Electrons. *Phys. Rev.* **1952**, *86*, 929.

35.   Lin, S., Rate of Interconversion of Electronic and Vibrational Energy. *J. Chem. Phys.* **1966**, *44*, 3759.

36.   Niu, Y.; Peng, Q.; Deng, C.; Gao, X.; Shuai, Z., Theory of Excited State Decays and Optical Spectra: Application to Polyatomic Molecules. *J. Phys. Chem. A* **2010**, *114*, 7817-7831.

37.   Shizu, K.; Adachi, C.; Kaji, H., Effect of Vibronic Coupling on Correlated Triplet Pair Formation in the Singlet Fission Process of Linked Tetracene Dimers. *J. Phys. Chem. A* **2020**, *124*, 3641-3651.

38.   Shizu, K.; Adachi, C.; Kaji, H., Visual Understanding of Vibronic Coupling and Quantitative Rate Expression for Singlet Fission in Molecular Aggregates. *Bull. Chem. Soc. Jpn.* **2020**, *93*, 1305-1313.

39.   Camposeo, A.; Polo, M.; Tavazzi, S.; Silvestri, L.; Spearman, P.; Cingolani, R.; Pisignano, D., Polarized Superradiance from Delocalized Exciton Transitions in Tetracene Single Crystals. *Phys. Rev. B* **2010**, *81*, 033306.

40.   Kolomeisky, A. B.; Feng, X.; Krylov, A. I., A Simple Kinetic Model for Singlet Fission: A Role of Electronic and Entropic Contributions to Macroscopic Rates. *J. Phys. Chem. C* **2014**, *118*, 5188-5195.

41.   Koseki, S.; Schmidt, M. W.; Gordon, M. S., MCSCF/6-31G(d,p) Calculations of One-Electron Spin-Orbit Coupling Constants in Diatomic Molecules. *J. Phys. Chem.* **1992**, *96*, 10768-10772.

42.   Kim, I.; Jeon, S. O.; Jeong, D.; Choi, H.; Son, W.-J.; Kim, D.; Rhee, Y. M.; Lee, H. S., Spin–Vibronic Model for Quantitative Prediction of Reverse Intersystem Crossing Rate in Thermally Activated Delayed Fluorescence Systems. *J. Chem. Theory Comput.* **2020**, *16*, 621-632.

43.   Gibson, J.; Monkman, A. P.; Penfold, T. J., The Importance of Vibronic Coupling for Efficient Reverse Intersystem Crossing in Thermally Activated Delayed Fluorescence Molecules. *ChemPhysChem* **2016**, *17*, 2956-2961.

44.   Minaev, B.; Minaeva, V.; Ågren, H., Theoretical Study of the Cyclometalated Iridium(Iii) Complexes Used as Chromophores for Organic Light-Emitting Diodes. *J. Phys. Chem. A* **2009**, *113*, 726-735.

45.   Li, X.; Minaev, B.; Ågren, H.; Tian, H., Density Functional Theory Study of Photophysical Properties of Iridium(Iii) Complexes with Phenylisoquinoline and Phenylpyridine Ligands. *J. Phys. Chem. C* **2011**, *115*, 20724-20731.

46.   Minaev, B.; Baryshnikov, G.; Agren, H., Principles of Phosphorescent Organic Light Emitting Devices. *Phys. Chem. Chem. Phys.* **2014**, *16*, 1719-1758.

47.   Toptygin, D., Effects of the Solvent Refractive Index and Its Dispersion on the Radiative Decay Rate and Extinction Coefficient of a Fluorescent Solute. *J. Fluoresc.* **2003**, *13*, 201-219.

48.   El-Sayed, M. A., Triplet State. Its Radiative and Nonradiative Properties. *Acc. Chem. Res.* **1968**, *1*, 8-16.

TOC graphic
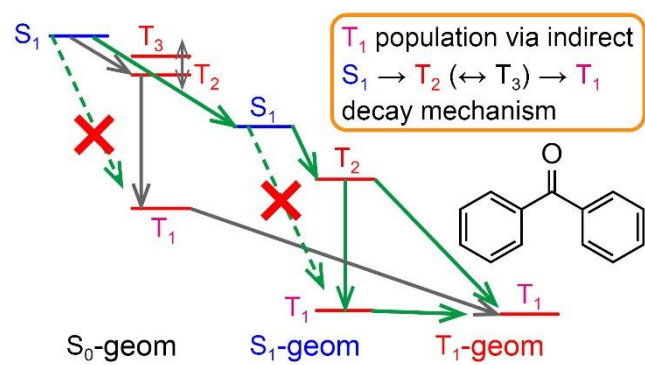
Brief description for TOC graphic

$S_1 \rightarrow T_2 (\leftrightarrow T_3) \rightarrow T_1 \rightarrow S_0$ is the predominant decay pathway of benzophenone.